Electronic Supplementary Material (ESI) for Journal of Materials Chemistry A.

## Supporting Information

# Sequentially Optimizing Carbon Nanotubes Framework towards Flexible and Compact Capacitive Energy Storage

Qing Yin,[a,#]Mingyu Ye,[a,#] Hongbing Jia,*[a] Antonio Arcanjo de Araújo Melo,[b] Qingmin Ji[c]

*a) Key Laboratory for Soft Chemistry and Functional Materials of Ministry of Education, Nanjing University of Science and Technology, Nanjing 210094, China*

*b) São Carlos Institute of Chemistry, University of São Paulo, São Paulo 13560-970, Brazil*

*c) Herbert Gleiter Institute of Nanoscience, Nanjing University of Science and Technology, Nanjing 210094, China*

Corresponding author: H. Jia (E-mail: polymernjust@gmail.com)

[#] The authors contributed equally to this work

## 1. Experimental Section

### 1.1. Materials

Single-walled carbon nanotubes (SWCNTs, average diameter of ~ 1.4 nm) used in the present work were synthesized by electric arc discharge and purchased from Carbon Solutions, Inc. Kevlar 49 yarns were purchased from DuPont de Nemours, Inc., and used after dried at 50 °C in vacuum for 12 h. Dimethyl sulfoxide (DMSO), potassium hydroxide (KOH), sodium dodecyl benzene sulfonate (SDBS), aniline monomer, polyvinyl alcohol (PVA, $M_w$ ~ 145000), sulfuric acid ($H_2SO_4$, 95 ~ 98 wt%) and hydrochloric acid (HCl, 36 ~ 38 wt%) were purchased from Sinopharm Chemical Reagent Co., Ltd. All reagents were of analytical grade and used as received without further purification. Water was purified by deionization and filtration with a Millipore purification apparatus (18.2 MΩ·cm).

### 1.2. Preparation of ANFs Dispersion and CNTs Ink

ANFs dispersion was prepared according to the method reported by Kotov's group.[1] Briefly, 1.0 g of Kevlar 49 yarns and 1.5 g of KOH were added into 100 mL of DMSO. After stirring for three weeks at room temperature, a dark red ANFs/DMSO dispersion (10 mg $mL^{-1}$) was obtained. To form a CNTs ink, SWCNTs were pre-treated at 350 ºC and purified with 6 M HCl, and then dispersed in water with assistance of SDBS. After bath sonication for 30 min (Elmasonic S30H), the CNTs dispersion was further probe-sonicated for 30 min at 350 W (Scientz-IID). The dispersion was centrifuged at 8000 rpm for 30 min, resulting in a stable CNTs ink with CNTs and SDBS concentrations of 0.2 and 1 mg $mL^{-1}$, respectively.

### 1.3. Self-Assembly of CNTs@ANFs Film Electrode

CNTs@ANFs film electrode was constructed by a two-step vacuum-assisted flocculation technique. Firstly, a desired amount of water was added into 15 mL of diluted ANFs dispersion (2 mg $mL^{-1}$) to re-protonate the amide groups of ANFs and form hydrogen bonding between ANFs, resulting in the formation of a gel-like system. After stirring vigorously for 2 h, the as-obtained dispersion was vacuum-filtered on a nylon membrane (0.22 µm pore size) to form a gel film. The filtered ANFs gel film was rinsed with water three times to eliminate impurities. Subsequently, the CNTs ink was poured onto the ANFs gel film and vacuum-filtered to form a typically double-layer architecture, followed by washing with a large amount of water to remove SDBS. Finally, the air-dried CNTs@ANFs film was peeled off from the filter membrane and dried at 60 ºC in vacuum for 3 days.

### 1.4. Electrochemical Enhancement of CNTs@ANFs Film Electrode

Electrooxidation of CNTs@ANFs film was carried out in 1 M $H_2SO_4$ using a three-electrode system, in which platinum foils and Ag/AgCl electrode were used as counter and reference electrodes, respectively. The film sample (CNTs mass loading of 1 mg $cm^{-2}$) was cut into the rectangular strips of 15 mm × 10 mm using a razor blade, and used as the working electrode. The oxidation process was performed with an Autolab-PGSTAT 302F workstation (Metrohm, Switzerland) at a constant potential of 2.2 V, and magnetic stirring was carried out during the process. Then, the functionalized sample was rinsed with water and dried at 60 ºC in vacuum for several minutes. Thermal annealing of the film sample was conducted using a muffle furnace at 200 ºC in air.

### 1.5. Preparation of PANI@CNTs@ANFs Film Electrode

PANI was synthesized by electrochemical oxidation polymerization of aniline in the presence of CNTs@ANFs film. Beforehand, the aniline monomer was dissolved in 1 M HCl aqueous solution to form an initial concentration of 0.3 M. Anodic deposition was performed with an Autolab-PGSTAT 302F workstation (Metrohm, Switzerland) using a three-electrode system, in which the functionalized CNTs@ANFs film, platinum foils and Ag/AgCl electrode were used as working, counter and reference electrodes, respectively. The distance between the working electrode and counter electrode was fixed at 15 mm. A constant potential of 0.8 V was first applied for 1 min to induce the nucleation of PANI at room temperature. Subsequently, a constant current density of 0.25 mA $cm^{-2}$ was used for the growth of PANI. In order to promote aniline monomer to diffuse into the interior of CNTs coating, magnetic stirring was maintained during the electrochemical deposition process. The resultant composite film was rinsed with 1M HCl, ethanol, and water successively. Finally, the composite film was re-doped in 1 M HCl for 1 h, then rinsed and dried at 40 ºC in vacuum overnight. For the sake of measuring the mass loading of PANI nanostructure on the film electrode, the prepared composite film was de-doped with 1 M ammonia water thoroughly and rinsed by water. The de-doped composite film was dried at 60 ºC in vacuum for 12 h, before weighing and calculating.

### 1.6. Fabrication of Flexible All-Solid-State Supercapacitor

All-solid-state supercapacitor device using the PANI@CNTs@ANFs films as freestanding electrodes were assembled in a symmetrical two-electrode configuration. Typically, a PVA/ $H_2SO_4$ gel electrolyte was prepared by mixing 2 g PVA powder and 2 g $H_2SO_4$ into 20 mL water. The mixture was heated to 85 ºC under vigorous stirring until the solution became clear. The cooled PVA/$H_2SO_4$ electrolyte was cast onto the as-prepared PANI@CNTs@ANFs films and dried at room temperature. Lastly, two pieces of working electrodes were assembled into a symmetrical device by using PVA/$H_2SO_4$ gel membrane as electrolyte and separator.

### 1.7. Characterizations

Atomic force microscopy (AFM) was carried out on a Multimode 8 atomic force microscope (Bruker, GER) in a tapping mode. The ANFs dispersion was spin-coated on a freshly exfoliated mica substrate at 2000 rpm and dried at room temperature. Transmission electron microscopy (TEM) was performed with a JEOL-2100 transmission electron microscope (JEOL, JPN) with an accelerating voltage of 200 kV. Scanning electron microscopy (SEM) was carried out using a JSM-IT500HR (JEOL, JPN) and a Nova NanoSEM 450 (FEI, USA) field-emission scanning electron microscopes. Fourier transform infrared (FT-IR) spectra were recorded on a Nicolet 8700 spectrometer (ThermoFisher Scientific, USA) at a scanning resolution of 2 $cm^{-1}$ in the wavenumber range from 4000 to 500 $cm^{-1}$. X-ray diffraction patterns (XRD) were recorded by a LabX XRD-6000 X-ray diffractometer (Shimadzu, JPN) with Cu K$\alpha$ radiation ($\lambda$ = 1.54184 Å) from 5 to 50 º, the scanning speed was 5 º $min^{-1}$. Raman spectra were collected on a LabRAM HR800 instrument (Horiba Jobin Yvon, FRA) using a 633 nm wavelength laser. X-ray photoelectron spectroscopy (XPS) was investigated by a ESCALAB 250 photoelectron spectrometer (ThermoFisher Scientific, USA) equipped with a monochromatic Al K$\alpha$ X-ray source (1486.6 eV). All spectra were calibrated with the C 1s photoemission peak centered at 284.6 eV, and the curve fitting of the photoemission spectra was performed on the basis of a Shirley type background subtraction. Thermogravimetric analysis (TGA) was carried out on a TGA 55 thermogravimetric analyzer (TA, USA) with a heating rate of 10 ºC $min^{-1}$ from 30 ºC to 800 ºC under a $N_2$ atmosphere. Sheet resistance was measured using Keithley 2400 multiple-function source-meter (Keithley, USA) with a four-probe method at room temperature. The results were averaged based on five independent measurements. Stress-strain test was performed on an Instron 4465 universal testing machine (Instron, USA) at room temperature with a humidity of about 25%. The sample was cut into the rectangular strips of 30 mm × 3 mm using a razor blade. The initial gauge length was 20 mm with a crosshead speed of 0.5 mm $\text{min}^{-1}$. The results were averaged based on five independent measurements. Electrochemical measurements were carried out on an Autolab-PGSTAT 302F workstation (Metrohm, Switzerland) using a three-electrode system, in which platinum foils and Ag/AgCl electrode were used as counter and reference electrodes, respectively. Electrochemical impedance spectroscopy (EIS) was recorded at open circuit potential with a frequency range from 100 kHz to 0.01 Hz under an oscillation potential amplitude of 10 mV. Areal specific capacitance ($C_\text{a}$, F $\text{cm}^{-2}$) and volumetric specific capacitance ($C_\text{v}$, F $\text{cm}^{-3}$) of single electrode and device were derived from the galvanostatic charge-discharge (GCD) curves using the following formulas:

$$C_\text{a} = \frac{I \times t}{\Delta U \times A} \#(1)$$

$$C_\text{v} = \frac{I \times t}{\Delta U \times V} \#(2)$$

where $I$ is the discharge current (A), $t$ is the discharge time (s), $\Delta U$ is the potential window after excluding the IR drop (V), $A$ is the geometric electrode working area ($\text{cm}^2$), and $V$ is the volume of working electrode ($\text{cm}^3$, including the inactive ANFs film substrate). For the all-solid-state supercapacitor device, $A$ is the geometric electrode working area ($\text{cm}^2$), $V$ is the volume of the entire device including two film electrodes and gel separator ($\text{cm}^3$). Volumetric energy density ($E_\text{v-stack}$, Wh $\text{cm}^{-3}$) and power density ($P_\text{v-stack}$, W $\text{cm}^{-3}$) of the entire device were obtained from:

$$E_\text{v - stack} = \frac{1}{2} \times \frac{C_v \times U^2}{3600} \#(3)$$

$$P_\text{v - stack} = \frac{E_\text{v - stack} \times 3600}{t} \#(4)$$

where $C_\text{v}$ is the volumetric specific capacitance of the entire device (F $\text{cm}^{-3}$), $U$ is the working voltage, and $t$ is the discharge time.

Additionally, the average discharge current ($I_\text{d}$, A $\text{cm}^{-2}$) of CNTs@ANFs film electrode at the specific scan rate is calculated based on the following formula:

$$I_d = \frac{A}{2 \times \Delta U} = \frac{\int_0^{0.8} I \times dU}{2 \times \Delta U}\#(5)$$

where $A$ is the integrated area of the CV curve at specific scan rate, and $\Delta U$ is the voltage window (0 ~ 0.8 V).

For the CNTs@ANFs film electrode, the real part ($C'$, F $cm^{-2}$) and the imaginary part ($C''$, F $cm^{-2}$) of the capacitance derived from EIS in the range of 100 ~ 0.01 Hz was obtained by using the formulas:

$$C'(\omega) = \frac{-Z''(\omega)}{\omega \times |Z(\omega)|^2}\#(6)$$

$$C''(\omega) = \frac{Z'(\omega)}{\omega \times |Z(\omega)|^2}\#(7)$$

where ω is the angular frequency (rad $s^{-1}$, $2\pi f$), $Z$ is the electrochemical impedance (Ω $cm^{-2}$), $Z'$ and $Z''$ are the real part and the imaginary part of $Z$, respectively.

## 2. Supporting Figures

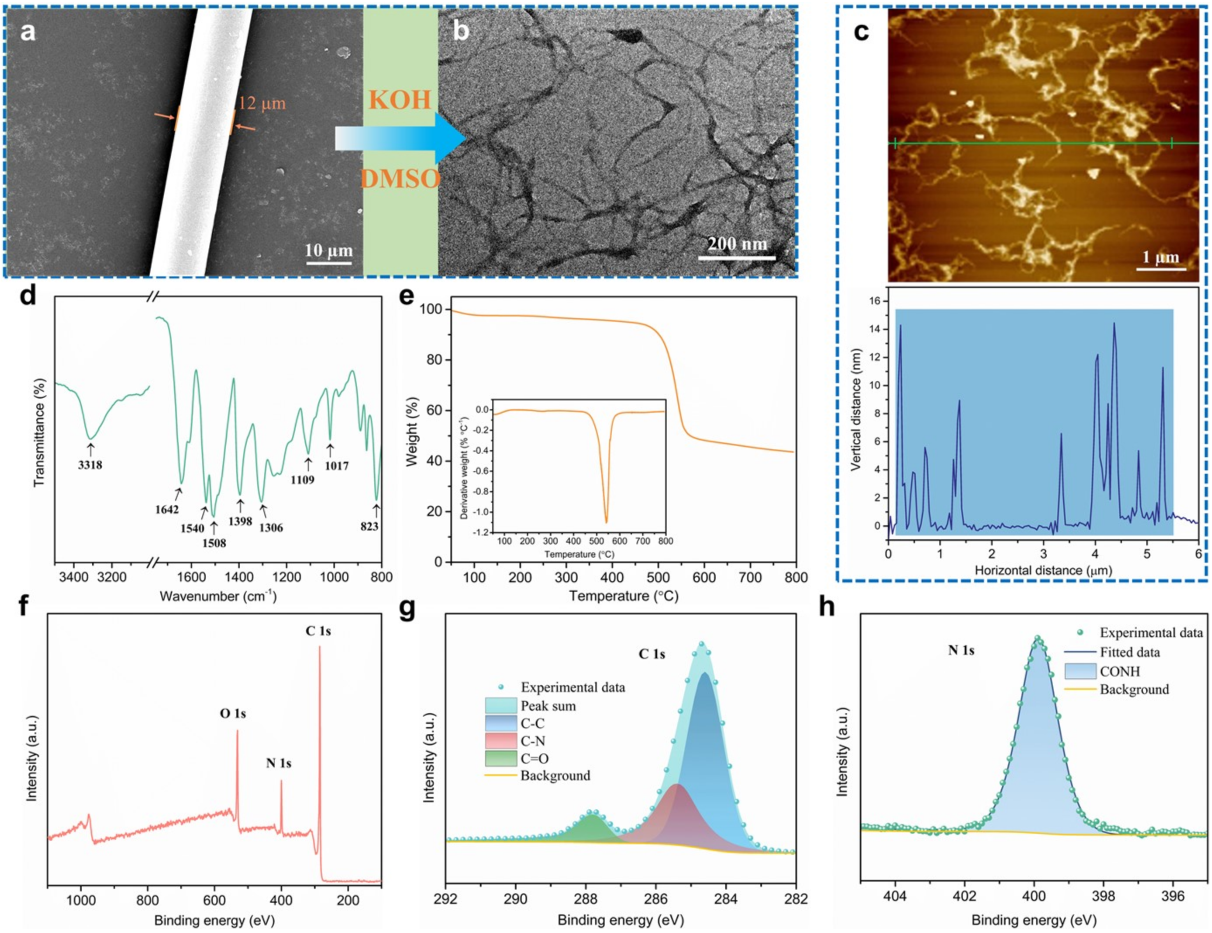

**Fig. S1** Micromorphology of ANFs and structural characterizations of ANFs film. (a) SEM image of Kevlar microfiber with a diameter of ~ 12 μm. (b) TEM image of ANFs. (c) AFM image of ANFs on mica, and the width distribution derived from cross section analysis showing that the diameters of ANFs are 5 ~ 15 nm. (d) FT-IR spectrum of ANFs film. The two obvious peaks at 3318 and 1642 cm$^{-1}$ are assigned to the N-H stretching vibration and C=O stretching vibration of amide group, respectively. The peak 1540 cm$^{-1}$ are ascribed to the N-H deformation and the C-N stretching coupled modes. The bands at 1508 and 1306 cm$^{-1}$

are attributed to the C=C stretching vibration of aromatic ring and Ph-N stretching vibration, respectively. The absorption bands originating from the in-plane and out-of-plane bending vibrations of C-H are located at 1017 and 823 cm$^{-1}$, respectively. The remaining absorption bands correspond well to previous literatures,[1-4] and together identify the molecular structures of ANFs in the film. (e) TGA curve and DTG curve (inset) of ANFs film. By virtue of the symmetric and ordered aromatic rings in the backbone unit of ANFs, the film shows obvious weight losses starting from 450 ºC, and the maximum decomposition temperature appears at 542 ºC. (f-h) XPS spectra of ANFs film with survey scan spectrum (f), high-resolution XPS C 1s spectrum (g), and high-resolution XPS N 1s spectrum (h). The C 1s spectrum is deconvolved into three characteristic peaks at 284.6, 285.3, and 287.8 eV, assigning to C(sp$^2$)-C(sp$^2$), C-N, and C=O, respectively.[5] A single Gaussian peak centered at 399.9 eV in N 1s spectrum confirms the existence of amide group.[5]

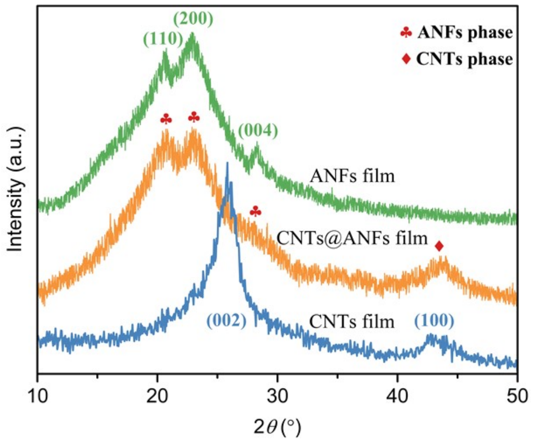

**Fig. S2** XRD patterns for ANFs, CNTs, and CNTs@ANFs films. The observed three broad peaks for the ANFs film are assigned to (110), (200), and (004) diffractions, respectively.[3, 6, 7] These characteristic Kevlar peaks signify the reservation of the crystalline PPTA structures in the nanoscale assembly, which is also indicative of the high mechanical properties for the ANFs film, inheriting from Kevlar fibers. The XRD pattern of the CNTs film exhibits two typical diffraction peaks in the vicinity of $2\theta$ = 26º and 43º, corresponding to the (002) reflection of graphitic carbon and the (100) reflection of turbostratic carbon, respectively.[8, 9] Distinctly, the diffractogram of the CNTs@ANFs sample testifies the presence of both ANFs and CNTs phases in the composite film. The inconspicuous change in the crystallinity of ANFs film indicates that the CNTs coating does not interfere with the crystalline structure of ANFs film.

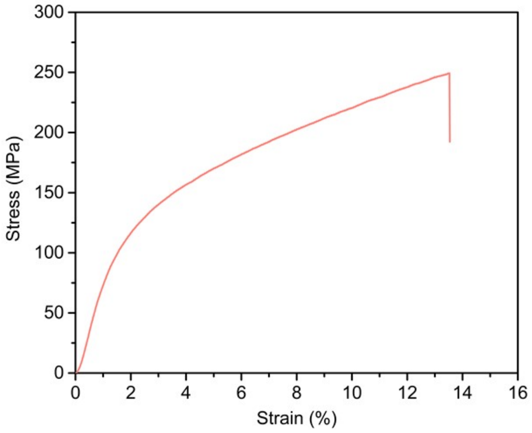

**Fig. S3** Typical stress-strain curve for ANFs film.

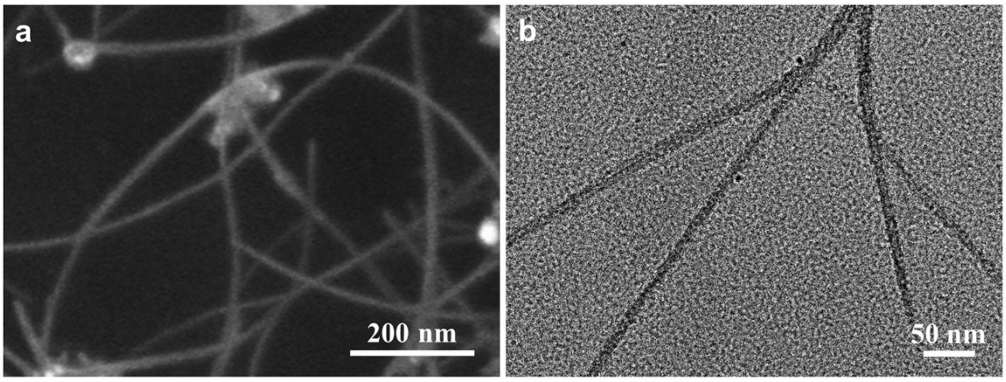

**Fig. S4** Micromorphology of SWCNTs. (a) SEM image and (b) TEM image.

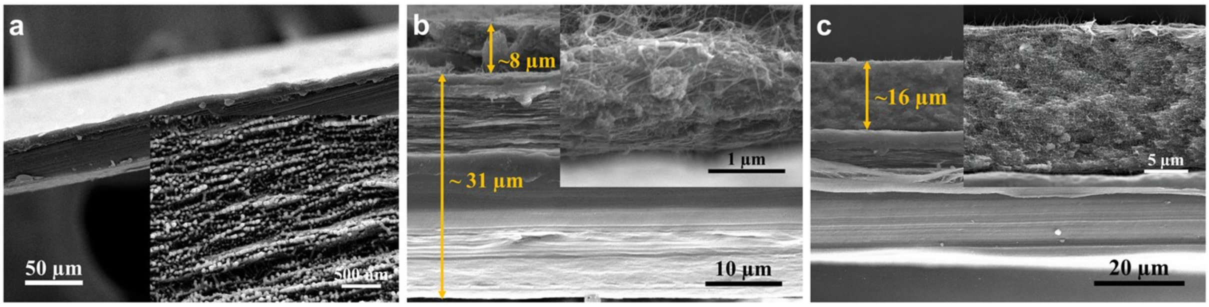

**Fig. S5** Front view SEM images of the cross-section for films. (a) ANFs film. (b, c) CNTs@ANFs composite film with CNTs mass loading of 1 mg cm$^{-2}$ (b) and 2 mg cm$^{-2}$ (c), suggesting the formation of high-quality interface.

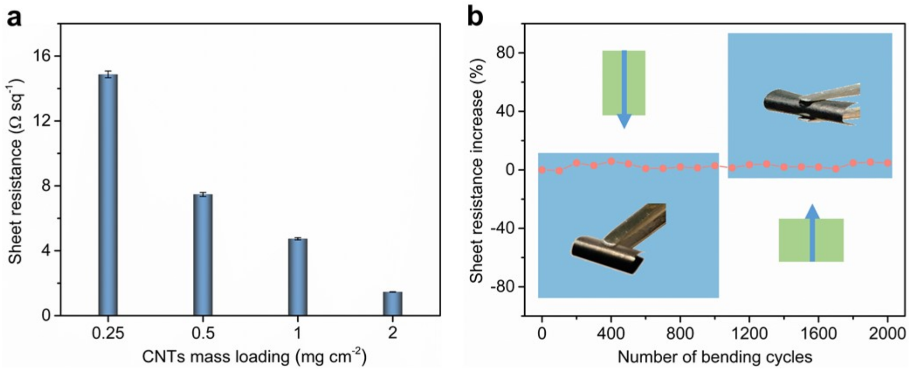

**Fig. S6** Conductive properties of CNTs@ANFs composite films. (a) Sheet resistance for composite films with different CNTs mass loadings. (b) Chang of electrical resistance *vs.* bending cycles for composite film with CNTs mass loading of 1 mg cm$^{-2}$.

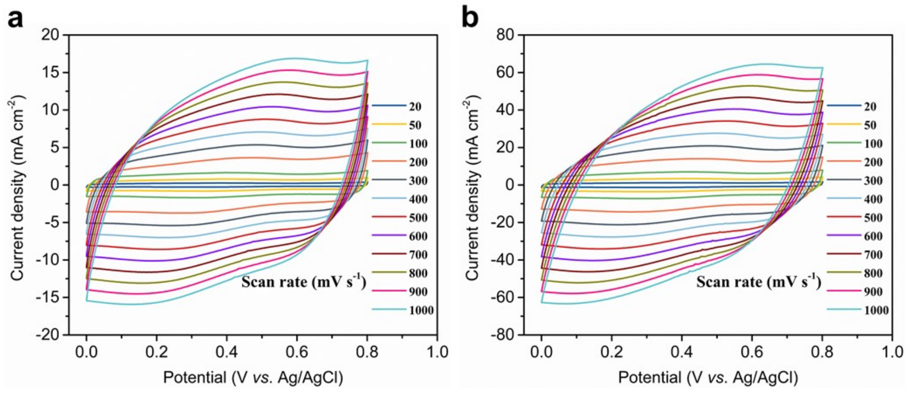

**Fig. S7** CV curves (20 ~ 1000 mV $s^{-1}$) for CNTs@ANFs film electrodes. (a) CNTs loading of 0.5 mg $cm^{-2}$. (b) CNTs loading of 2 mg $cm^{-2}$.

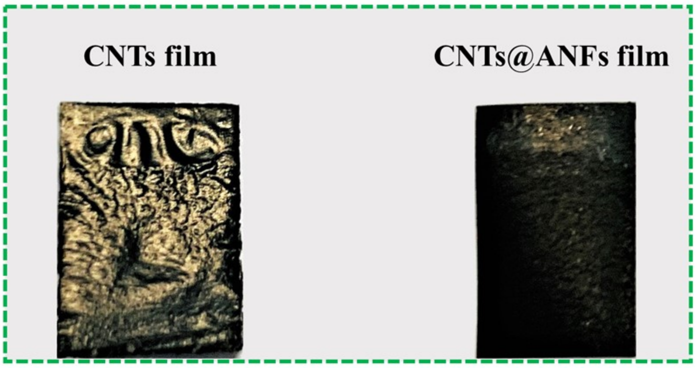

**Fig. S8** Photographs for a comparison of composite film with pure SWCNTs film, after being treated with 30 s of electrooxidation and 5 min of annealing. The composite film maintains excellent structure stability while pure SWCNTs film suffers from severe deformation and cannot even support itself.

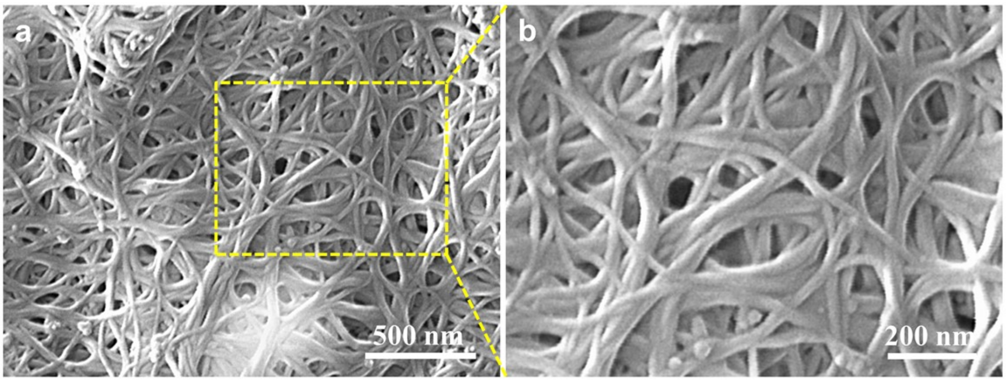

**Fig. S9** SEM image of the double-layer CNTs@ANFs film electrode after 30 s of electrooxidation followed by 5 min of annealing.

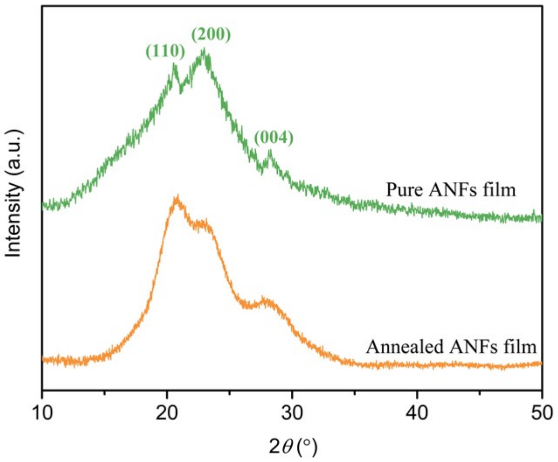

**Fig. S10** XRD patterns of the ANFs film before and after annealing treatment.

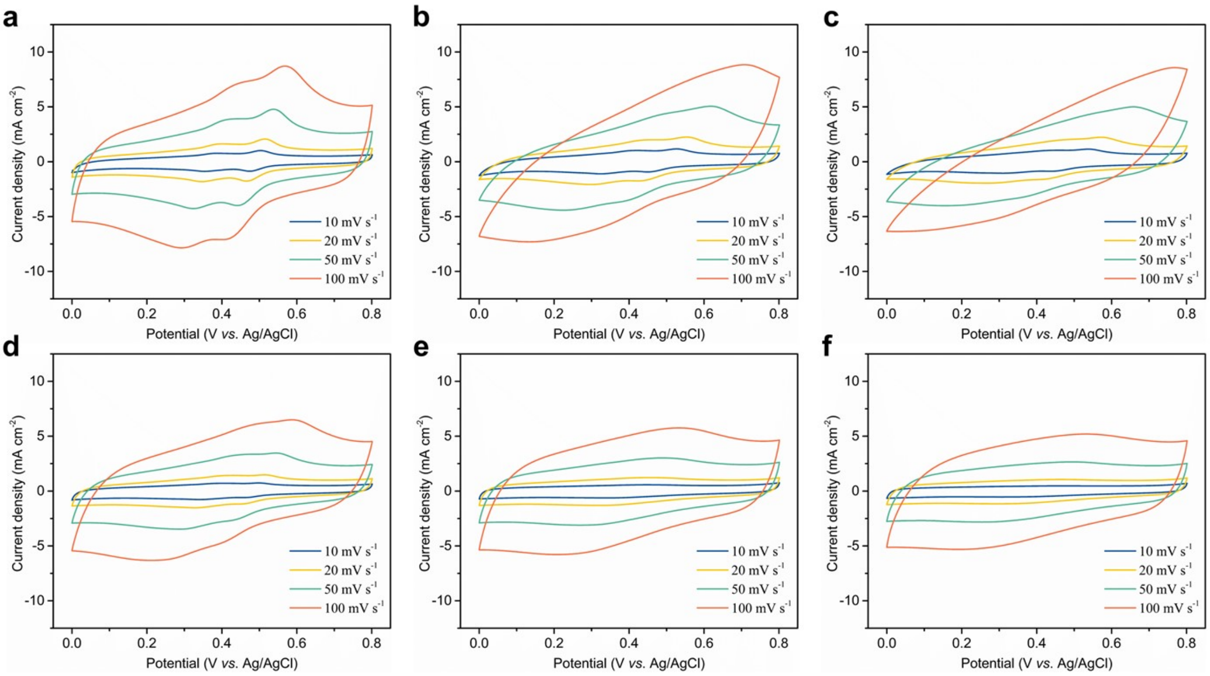

**Fig. S11** CV curves (10 ~ 100 mV $s^{-1}$) for CNTs@ANFs film electrodes after electrochemical enhancement. (a-c) Film electrode electrooxidized with 15 s (a), 60 s (b), and 90 s (c), followed by thermal annealing for 5 min. (d-f) Film electrode electrooxidized with 30 s followed by thermal annealing for 10 min (d), 30 min (e), and 60 min (f).

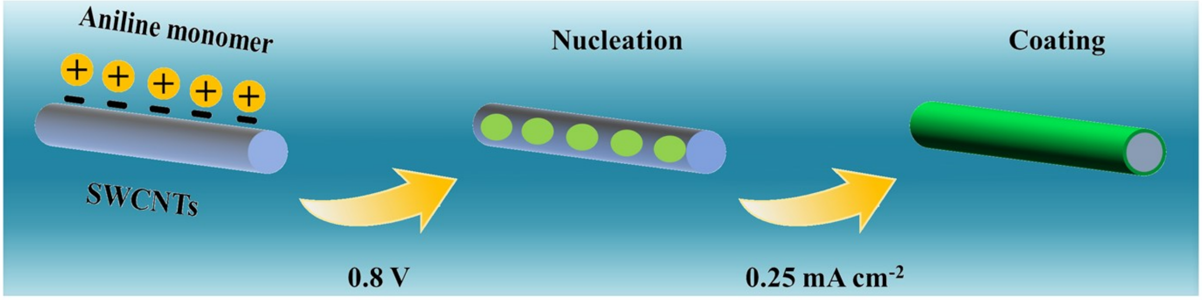

**Fig. S12** Schematic illustration for the formation of PANI on CNTs. A constant potential of 0.8 V was first applied for 1 min to induce the nucleation of PANI, after that a small constant current density of 0.25 mA cm$^{-2}$ was applied to coat PANI uniformly on CNTs surface.

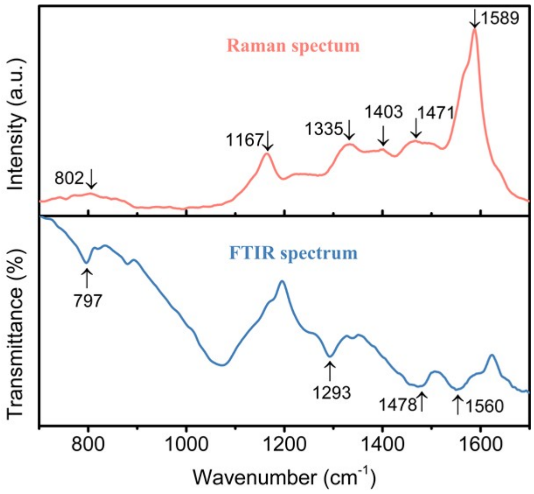

**Fig. S13** FT-IR (blue) and Raman (red) spectra for PANI@CNTs@ANFs film electrode.

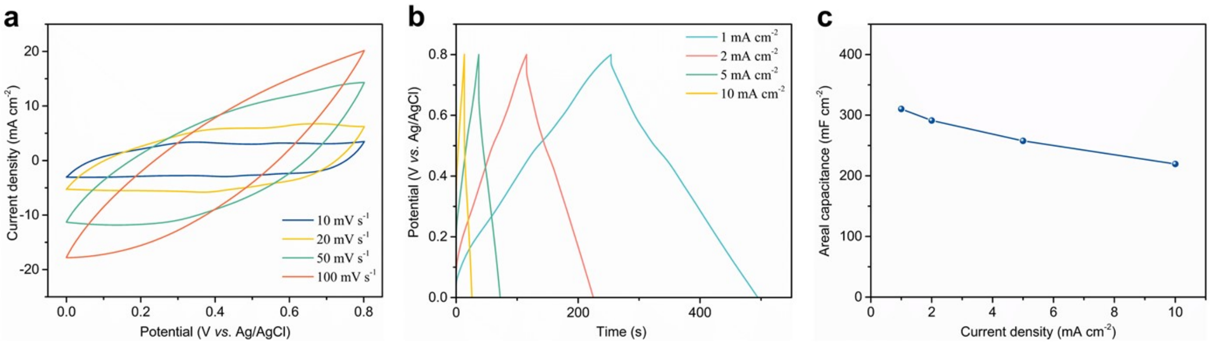

**Fig. S14** Electrochemical characterization of PANI@CNTs@ANFs film electrode with PANI deposition time of 60 min. (a) CV curves at different scan rates (10 ~ 100 mV s$^{-1}$). (b) GCD curves at different current densities (0.5 ~ 10 mA cm$^{-2}$). (c) Areal capacitances obtained at different discharge current densities.

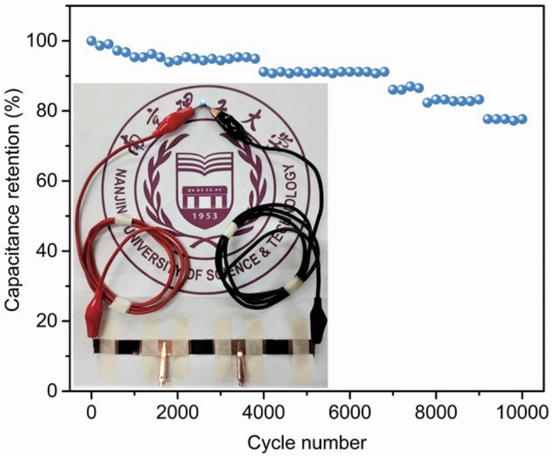

**Fig. S15** Cycling stability of PANI@CNTs@ANFs-based solid-state supercapacitor.

## 3. Supporting Tables

**Table S1.** The sheet resistance of CNTs@ANFs films and previously reported electrodes prepared by loading active materials on inactive substrates.

| Electrode material (freestanding) | Sheet resistance (Ω $sq^{-1}$) | Ref. |
|---|---|---|
| SWCNTs coated wiper cloth | 60 | [10] |
| Tin-doped indium oxide coated paper | 12 | [11] |
| Au coated paper | 7 | [12] |
| DWCNTs coated bacterial cellulose film | 7 | [13] |
| PEDOT coated paper | 5.5 | [14] |
| SWCNTs coated cotton fabrics | 1 ~ 4 | [15] |
| CNTs@ANFs film (0.25 mg $cm^{-2}$) | 14.9 | This work |
| CNTs@ANFs film (0.50 mg $cm^{-2}$) | 7.5 | This work |

| | | |
|---|---|---|
| CNTs@ANFs film (1.00 mg cm$^{-2}$) | 4.7 | This work |
| CNTs@ANFs film (2.00 mg cm$^{-2}$) | 1.5 | This work |

**Table S2.** The assignment of Kevlar active modes (Raman scattering).

| Wavenumber (cm$^{-1}$) | Assignment |
|---|---|
| 1182 | C-C ring stretching |
| 1277 | C-C ring stretching |
| 1327 | C-H in-plane bending |
| 1510 | C-C ring stretching |
| 1568 | N-H bending, C-N stretching |
| 1610 | C-C ring stretching |
| 1649 | C=O stretching |

**Table S3.** Mechanical properties for CNTs@ANFs films, pure SWCNTs film and ANFs film.

| Sample | Tensile strength (MPa) | Modulus (GPa) | Toughness (MJ $m^{-3}$) |
|---|---|---|---|
| SWCNTs film | 16.8 ± 0.5 | 2.0 ± 0.1 | 0.23 ± 0.03 |
| CNTs@ANFs film (0.25 mg $cm^{-2}$) | 275.7 ± 4.5 | 10.6 ± 0.6 | 27.6 ± 2.2 |
| CNTs@ANFs film (0.50 mg $cm^{-2}$) | 234.7 ± 6.9 | 9.3 ± 0.7 | 23.4 ± 2.9 |
| CNTs@ANFs film (1.00 mg $cm^{-2}$) | 209.6 ± 4.3 | 9.0 ± 0.8 | 18.3 ± 1.7 |
| CNTs@ANFs film (2.00 mg $cm^{-2}$) | 170.3 ± 3.9 | 7.9 ± 0.6 | 11.5 ± 0.8 |
| ANFs film | 257.1 ± 7.1 | 8.5 ± 0.5 | 25.3 ± 1.2 |

**Table S4.** The assignment of PANI active modes (Raman scattering).

| Wavenumber (cm$^{-1}$) | Assignment |
|---|---|
| 802 | C-H out-of-plane bending |
| 1167 | C-H in-plane bending |
| 1335 | C-N$^{+\cdot}$ stretching of bipolaron structure |
| 1403 | C=N stretching |
| 1471 | C=C stretching of benzenoid ring |
| 1589 | C=C stretching of quinoid ring |

**Table S5.** The assignment of PANI absorption bands (FT-IR spectrum).

| Wavenumber ($cm^{-1}$) | Assignment |
|---|---|
| 797 | C-H out-of-plane bending |
| 1293 | C-N stretching of secondary aromatic amine |
| 1478 | C=C stretching of benzenoid ring |
| 1560 | C=C stretching of quinoid ring |

**Table S6.** Comparison of capacitive performances for pseudocapacitive electrodes assembled by various methods.

| Electrode material (flexible) | Preparation method | Test condition | Specific capacitance (mF $cm^{-2}$) | Rate capability | Ref. |
|---|---|---|---|---|---|
| PPy/rGO membrane | Blending | 10 mV $s^{-1}$ | 175 | ~70% (400 mV $s^{-1}$) | 16 |
| $WS_2$/rGO film | Blending | 0.25 mA $cm^{-2}$ | 241.2 | 61% (5 mA $cm^{-2}$) | 17 |
| $MnO_2$/rGO fiber | Blending | 0.06 mA $cm^{-3}$ | 82.6 | 62.2% (0.97 mA $cm^{-3}$) | 18 |
| $MnO_2$/rGO film | Blending | 0.1 A $g^{-1}$ | 802 | ~37% (1 A $g^{-1}$) | 19 |
| N-doped rGO/$MnO_2$ film | Blending | 0.25 A $g^{-1}$ | 430 | 69.2% (2 A $g^{-1}$) | 20 |
| PANI/CNTs@cellulose paper | Dipping deposition | 0.2 mA $cm^{-2}$ | 330 | 75% (2 mA $cm^{-2}$) | 21 |
| SDBS-PPy@filter paper | Dipping deposition | 2 mV $s^{-1}$ | 438 | 54% (200 mV $s^{-1}$) | 22 |
| PPy@carbon aerogel | Dipping deposition | 1 mA $cm^{-2}$ | 419 | ~36% (20 mA $cm^{-2}$) | 23 |
| PANI@rGO@cotton yarn | Dipping deposition | 5 mV $s^{-1}$ | 246 | ~25% (100 mV $s^{-1}$) | 24 |
| PPy@rGO@cellulose film | Dipping deposition | 0.5 mA $cm^{-2}$ | 363 | ~62% (2 mA $cm^{-2}$) | 25 |

| | | | | | |
|---|---|---|---|---|---|
| MnO$_2$@CNTs@G foam | Dipping deposition | 5 mV s$^{-1}$ | ~730 | 12% (100 mV s$^{-1}$) | 26 |
| PANI/CNTs@PPW fabric | Dipping deposition | 1 mA cm$^{-2}$ | 386 | 60% (5 mA cm$^{-2}$) | 27 |
| Fe$_2$O$_3$/PPy@ carbon cloth | Vapor-phase polymerization | 0.5 mA cm$^{-2}$ | 382.7 | 31.6% (6 mA cm$^{-2}$) | 28 |
| PEDOT@ carbon cloth | vapor-phase polymerization | 1 mA cm$^{-2}$ | 201.4 | 64.4% (10 mA cm$^{-2}$) | 29 |
| PANI@graphite foil | Electrochemical deposition | 0.5 mA cm$^{-2}$ | 437.9 | 83% (10 mA cm$^{-2}$) | 30 |
| PANI@CNTs/epoxy | Electrochemical deposition | 0.2 mA cm$^{-2}$ | 36 | 55.5% (2 mA cm$^{-2}$) | 31 |
| PEDOT/MnO$_2$@stainless steel yarn | Electrochemical deposition | 0.76 mA cm$^{-2}$ | 170 | 47% (5 mA cm$^{-2}$) | 32 |
| PANI@graphite@paper | Electrochemical deposition | 0.5 mA cm$^{-2}$ | 355.6 | ~70% (5 mA cm$^{-2}$) | 33 |
| PPy@CNTs@urethane yarn | Electrochemical deposition | 5 mV s$^{-1}$ | 308 | 82.8% (20 mV s$^{-1}$) | 34 |
| PPy@CNTs buckyaper | Electrochemical deposition | 1.4 mA cm$^{-2}$ | 280 | <45% (14 mA cm$^{-2}$) | 35 |
| This work | Electrochemical deposition | 0.5 mA cm$^{-2}$ | 462.4 | 77.0% (10 mA cm$^{-2}$) | |

Some of the rate values listed in the table are directly extracted from the data graphs in corresponding literature, and some errors are inevitable.

**Table S7.** Summary of capacitive performances of all-solid-state flexible supercapacitors with symmetric and asymmetric configurations (Volumetric capacitance is normalized to the volume of the entire device).

| Electrode material | Electrolyte | Test condition | Areal capacitance (mF cm$^{-2}$) | Volumetric capacitance (F cm$^{-3}$) | Ref. |
|---|---|---|---|---|---|
| MnO$_2$/C@carbon fabric | PVA/H$_3$PO$_4$ | 0.1 mA cm$^{-2}$ | 5.5 | 0.072 | 36 |
| TiO$_2$@carbon fiber | PVA/H$_2$SO$_4$ | 0.1 mA cm $^{-2}$ | 10 | 0.125 | 37 |
| TiN nanowire | PVA/KOH | 2.5 mA cm$^{-3}$ | 26.4 | 0.33 | 38 |
| MnO$_2$@graphene foam | Na$_2$SO$_4$ | 0.3 mA cm$^{-2}$ | 28.6 | 0.358 | 39 |
| CNTs/PANI yarn | PVA/H$_2$SO$_4$ | 0.01 mA cm$^{-2}$ | 38 | 3.17 | 40 |
| PANI@Au coated paper | PVA/H$_3$PO$_4$ | 0.2 mA cm$^{-2}$ | 50 | 2.08 | 12 |

| | | | | | |
|---|---|---|---|---|---|
| PPy@CNTs@urethane yarn | PVA/$H_3PO_4$ | 0.1 mA $cm^{-2}$ | 69 | 5.27 | [34] |
| PANI@graphite@paper | PVA/$H_2SO_4$ | 0.1 mA $cm^{-2}$ | 77.8 | 3.55 | [33] |
| PPy@CNTs buckyaper | PVA/$H_2SO_4$ | 50 mA $cm^{-3}$ | 122.5 | 4.9 | [35] |
| VN/CNTs film | PVA/$H_3PO_4$ | 25 mA $cm^{-3}$ | 110.6 | 7.9 | [41] |
| This work | PVA/$H_2SO_4$ | 0.25 mA $cm^{-2}$ | 149.8 | 9.4 | |

## 4. Supplementary Note

**Comprehensive comparison of CNTs@ANFs double-layered films with previously studied CNTs-based materials in the aspects of ultimate strength and Young′s modulus:**

We first compared the CNTs@ANFs film against neat CNTs buckypaper, considering the fact that both have the characteristics necessary for idea electrode materials, such as the consecutively porous nature and intact CNTs conductive network. The integrated mechanical properties of CNTs@ANFs film are far superior to that of SWCNTs and MWCNTs buckypaper prepared by either vacuum filtration[42, 43] or electrophoretic deposition (EPD),[44] outperforming by more than an order of magnitude in strength and 2.5 ~ 12 times in modulus. This makes our CNTs@ANFs film the strongest and stiffest porous CNTs electrode material made to date for electrochemical energy storage. Although the functionalization techniques of CNTs buckypaper by physical or chemical cross-linking have revealed efficient interfacial bonding among nanotubes network,[45] very few of them, in most cases, have produced comparably impressive mechanical performance, and probably not be the best answer to the question of load transfer improvement. In respect to strength, it is easy to see from the plot that the CNTs@ANFs films are much stronger than any reported non-covalent cross-linked CNTs buckypaper or film (PC,[46] PVA[47] and PSE-AP[48]) with the closest competitor being 150 MPa of covalent cross-linked SWCNTs buckypaper (PCDO).[49] To date, reinforcing SWCNTs buckypaper by grafting PCDO has been shown to be the most successful, which displays a modulus of 10.18 GPa, slightly higher than our CNTs@ANFs films. However, the destruction of the conductive network caused by the covalent modification of CNTs, which brings the sluggish electrochemical reactivity in the fast charge/discharge process, creates additional obstacles in achieving synergistic effects. While method that improve alignment of CNTs can optimize stress transfer between nanotubes, this method has resulted in moderate strength (94.62 MPa) and modulus (8.35 GPa) for aligned SWCNTs buckypaper.[50] The dense network with highly aligned CNTs eliminates the macro-porous structure in buckypaper, which is not feasible to retain its electrochemical activity (electrolyte shuttling) and further boost stack energy storage by loading pseudocapacitive substance.[50] We next compared the mechanical properties of CNTs@ANFs films with those of other CNTs/polymer composites consisting of randomly oriented CNTs. The present polymer matrices for CNT bulk composites include mostly thermoplastic (such as chlorinated polypropylene (CPP))[51] and thermosetting (such as epoxy)[52] polymers. Remarkably, the reported mechanical properties for SWCNTs/epoxy and SWCNTs/CPP composites are far worse than those of CNTs@ANFs films, mostly because of the poor performance of polymer substrates. The use of highly crystalline nylon[53] still does not endow the CNT-based composites with satisfactory mechanical performance, compared with our CNTs@ANFs films. Comparison against the MWCNTs/cellulose[54] and SWCNTs/PVA[55] composites further reveals that such excellent mechanical properties put the CNTs@ANFs films in a unique position among reported CNTs bulk composites with randomly oriented CNTs. An impressive example was reported for SWCNTs/cellulose, which delivered a strength of 250 MPa and a modulus of 12 GPa. However, the extremely low SWCNTs content (only 6.15 wt.%) make the hybrid film impossible to use as electrode materials.[54] Efforts toward the substantial improvement in mechanical performance have been taken with extensive work focusing on the uniaxial macro-fibers prepared by spinning techniques, such as SWCNTs/PVA[56] and SWCNTs/PAN.[57] Benefiting from the nearly perfect alignment of CNTs, these composite fibers achieved unusual mechanical properties especially in stiffness (exceeding 15 GPa, as shown in the plot). Such success in fact cannot be replicated in the development of advanced CNTs composite films, since the uniaxial fibers lack the isotropic distribution of stress and uniformity of electrical transport that typically exist in the composite films.[58]

## References

1. M. Yang, K. Cao, L. Sui, Y. Qi, J. Zhu, A. Waas, E. M. Arruda, J. Kieffer, M. Thouless and N. A. Kotov, *ACS Nano*, 2011, **5**, 6945-6954.
2. K. Cao, C. P. Siepermann, M. Yang, A. M. Waas, N. A. Kotov, M. D. Thouless and E. M. Arruda, *Adv. Funct. Mater.*, 2013, **23**, 2072-2080.
3. Q. Yin, H. Jia, A. Mohamed, Q. Ji and L. Hong, *Nanoscale*, 2020, **12**, 5507-5520.
4. J. Fan, Z. Shi, M. Tian and J. Yin, *RSC Adv.*, 2013, **3**, 17664-17667.
5. J. Zhu, W. Cao, M. Yue, H. Ying and M. Yang, *ACS Nano*, 2015, **9**, 2489-2501.
6. J. Fan, Z. Shi, L. Zhang, J. Wang and J. Yin, *Nanoscale*, 2012, **4**, 7046-7055.
7. P. Hu, J. Lyu, C. Fu, W. B. Gong, J. Liao, W. Lu, Y. Chen and X. Zhang, *ACS Nano*, 2020, **14**, 688-697.
8. Y. Yang, A. Centrone, L. Chen, F. Simeon, T. Alan Hatton and G. C. Rutledge, *Carbon*, 2011, **49**, 3395-3403.
9. J. A. Rojas, L. A. Ardila-Rodríguez, M. F. Diniz, M. Gonçalves, B. Ribeiro and M. C. Rezende, *Mater. Design*, 2019, **166**, 107612.
10. K. Wang, P. Zhao, X. Zhou, H. Wu and Z. Wei, *J. Mater. Chem.*, 2011, **21**, 16373-16378.
11. L. Hu, G. Zheng, J. Yao, N. Liu, B. Weil, M. Eskilsson, E. Karabulut, Z. Ruan, S. Fan, J. T. Bloking, M. D. McGehee, L. Wågberg and Y. Cui, *Energy Environ. Sci.*, 2013, **6**, 513-518.
12. L. Yuan, X. Xiao, T. Ding, J. Zhong, X. Zhang, Y. Shen, B. Hu, Y. Huang, J. Zhou and Z. L. Wang, *Angew. Chem. Int. Ed.*, 2012, **51**, 4934-4938.
13. Y. J. Kang, S. J. Chun, S. S. Lee, B. Y. Kim, J. H. Kim, H. Chung, S. Y. Lee and W. Kim, *ACS Nano*, 2012, **6**, 6400-6406.
14. J. Zhou, T. Fukawa, H. Shirai and M. Kimura, *Macromol. Mater. Eng.*, 2010, **295**, 671-675.
15. L. Hu, M. Pasta, F. L. Mantia, L. Cui, S. Jeong, H. D. Deshazer, J. W. Choi, S. M. Han and Y. Cui, *Nano Lett.*, 2010, **10**, 708-714.
16. J. Zhang, P. Chen, B. H. Oh and M. B. Chan-Park, *Nanoscale*, 2013, **5**, 9860-9866.
17. J. Li, K. Liao, X. Wang, P. Shi, J. Fan, Q. Xu and Y. Min, *Adv. Mater. Interfaces*, 2017, **4**, 1700419.
18. W. Ma, S. Chen, S. Yang, W. Chen, Y. Cheng, Y. Guo, S. Peng, S. Ramakrishna and M. Zhu, *J. Power Sources*, 2016, **306**, 481-488.
19. A. Sumboja, C. Y. Foo, X. Wang and P. S. Lee, *Adv. Mater.*, 2013, **25**, 2809-2815.
20. Y. Liu, X. Miao, J. Fang, X. Zhang, S. Chen, W. Li, W. Feng, Y. Chen, W. Wang and Y. Zhang, *ACS Appl. Mater. Interfaces*, 2016, **8**, 5251-5260.
21. D. Ge, L. Yang, L. Fan, C. Zhang, X. Xiao, Y. Gogotsi and S. Yang, *Nano Energy*, 2015, **11**, 568-578.
22. L. Huang, X. Yao, L. Yuan, B. Yao, X. Gao, J. Wan, P. Zhou, M. Xu, J. Wu, H. Yu, Z. Hu, T. Li, Y. Li and J. Zhou, *Energy Storage Mater.*, 2018, **12**, 191-196.
23. M. Yu, Y. Han, Y. Li, J. Li and L. Wang, *Carbohydr. Polym.*, 2018, **199**, 555-562.
24. C. Jin, H.-T. Wang, Y.-N. Liu, X.-H. Kang, P. Liu, J.-N. Zhang, L.-N. Jin, S.-W. Bian and Q. Zhu, *Electrochim. Acta*, 2018, **270**, 205-214.
25. S. Lyu, H. Chang, F. Fu, L. Hu, J. Huang and S. Wang, *J. Power Sources*, 2016, **327**, 438-446.
26. J. Liu, L. Zhang, H. B. Wu, J. Lin, Z. Shen and X. W. Lou, *Energy Environ. Sci.*, 2014, **7**, 3709-3719.
27. F. C. R. Ramirez, P. Ramakrishnan, Z. P. Flores-Payag, S. Shanmugam and C. A. Binag, *Synth. Met.*, 2017, **230**, 65-72.
28. L. Wang, H. Yang, X. Liu, R. Zeng, M. Li, Y. Huang and X. Hu, *Angew. Chem. Int. Ed.*, 2017, **56**, 1105-1110.

29. X. Zhao, M. Dong, J. Zhang, Y. Li and Q. Zhang, *Nanotechnology*, 2016, **27**, 385705.
30. H. Zhou, W. Zhang, X. Zhi and H.-J. Zhai, *J. Power Sources*, 2018, **402**, 311-319.
31. R. Wang, Q. Wu, X. Zhang, Z. Yang, L. Gao, J. Ni and O. K. C. Tsui, *J. Mater. Chem. A*, 2016, **4**, 12602-12608.
32. J. Sun, Y. Huang, C. Fu, Y. Huang, M. Zhu, X. Tao, C. Zhi and H. Hu, *J. Mater. Chem. A*, 2016, **4**, 14877-14883.
33. B. Yao, L. Yuan, X. Xiao, J. Zhang, Y. Qi, J. Zhou, J. Zhou, B. Hu and W. Chen, *Nano Energy*, 2013, **2**, 1071-1078.
34. J. Sun, Y. Huang, C. Fu, Z. Wang, Y. Huang, M. Zhu, C. Zhi and H. Hu, *Nano Energy*, 2016, **27**, 230-237.
35. Y. Chen, L. Du, P. Yang, P. Sun, X. Yu and W. Mai, *J. Power Sources*, 2015, **287**, 68-74.
36. L. Yuan, X. H. Lu, X. Xiao, T. Zhai, J. Dai, F. Zhang, B. Hu, X. Wang, L. Gong and J. Chen, *ACS Nano*, 2012, **6**, 656-661.
37. H. Zheng, T. Zhai, M. Yu, S. Xie, C. Liang, W. Zhao, S. C. I. Wang, Z. Zhang and X. Lu, *J. Mater. Chem. C*, 2013, **1**, 225-229.
38. X. Lu, G. Wang, T. Zhai, M. Yu, S. Xie, Y. Ling, C. Liang, Y. Tong and Y. Li, *Nano Lett.*, 2012, **12**, 5376-5381.
39. Y. He, W. Chen, X. Li, Z. Zhang, J. Fu, C. Zhao and E. Xie, *ACS Nano*, 2013, **7**, 174-182.
40. K. Wang, Q. Meng, Y. Zhang, Z. Wei and M. Miao, *Adv. Mater.*, 2013, **25**, 1494-1498.
41. X. Xiao, X. Peng, H. Jin, T. Li, C. Zhang, B. Gao, B. Hu, K. Huo and J. Zhou, *Adv. Mater.*, 2013, **25**, 5091-5097.
42. U. Dettlaff-Weglikowska, V. Skakalova, R. Graupner, S. Jhang, B. Kim, H. Lee, L. Ley, Y. Park, S. Berber and D. Tomanek, *J. Am. Chem. Soc.*, 2005, **127**, 5125-5131.
43. Y. Hu, D. Li, P. Tang, Y. Bin and H. Wang, *Mater. Design*, 2019, **184**, 108175.
44. J. L. Rigueur, S. A. Hasan, S. V. Mahajan and J. H. Dickerson, *Carbon*, 2010, **48**, 4090-4099.
45. B. S. Shim, J. Zhu, E. Jan, K. Critchley, P. Podsiadlo, S. Ho, K. Sun and N. A. Kotov, *ACS Nano*, 2009, **3**, 1711-1722.
46. G. T. Pham, Y. B. Park, S. Wang, Z. Liang, B. Wang, C. Zhang, P. Funchess and L. Kramer, *Nanotechnology*, 2008, **19**, 325705.
47. G. Xu, Q. Zhang, W. Zhou, J. Huang and F. Wei, *Appl. Phys. A*, 2008, **92**, 531-539.
48. I. W. Chen, *Chem. Commun.*, 2013, **49**, 2753-2755.
49. I. W. Chen, R. Liang, H. Zhao, B. Wang and C. Zhang, *Nanotechnology*, 2011, **22**, 485708.
50. J. Y. Oh, S. J. Yang, J. Y. Park, T. Kim, K. Lee, Y. S. Kim, H. N. Han and C. R. Park, *Nano Lett.*, 2015, **15**, 190-197.
51. Rowan, Blake, Yurii, K., Gun'ko, Jonathan, Coleman, Martin, Cadek and Antonio, *J. Am. Chem. Soc.*, 2004, **126**, 10226-10227.
52. J. Zhu, H. Peng, F. Rodriguez-Macias, J. L. Margrave, V. N. Khabashesku, A. M. Imam, K. Lozano and E. V. Barrera, *Adv. Funct. Mater.*, 2004, **14**, 643-648.
53. D. Z. Wei, S. Lu, I. Y. Phang and T. Liu, *Macromolecules*, 2004, **37**, 256-259.
54. H. Koga, T. Saito, T. Kitaoka, M. Nogi, K. Suganuma and A. Isogai, *Biomacromolecules*, 2013, **14**, 1160-1165.
55. L. Liu, A. H. Barber, S. Nuriel and H. D. Wagner, *Adv. Funct. Mater.*, 2005, **15**, 975-980.
56. B. Vigolo, A. Penicaud, C. Coulon, C. Sauder, R. Pailler, C. Journet, P. Bernier and P. Poulin, *Science*, 2000, **290**, 1331-1334.

57. T. V. Sreekumar, T. Liu, B. G. Min, H. Guo, S. Kumar, R. H. Hauge and R. E. Smalley, *Adv. Mater.*, 2004, **16**, 58-61.

58. S. Wan, Y. Li, J. Mu, A. E. Aliev, S. Fang, N. A. Kotov, L. Jiang, Q. Cheng and R. H. Baughman, *Proc. Natl. Acad. Sci. U. S. A.*, 2018, **115**, 5359-5364.